Gravitational and Coriolis forces in crystal neutron interferometry. II. Numerical simulations

(Article begins on next page)

18 January 2025

Gravitational and Coriolis forces in crystal neutron interferometry. II. Numerical simulations

E. Massa ⬤,* G. Mana ⬤,† and C. P. Sasso ⬤‡

Istituto Nazionale di Ricerca Metrologica, Strada delle Cacce 91, 10135 Torino, Italy

Previous studies have proven that neutron interference using split-crystal interferometers is possible. This proof paves the way for extended arm separation and length, opening the doors to new experiments exploring quantum mechanics and gravity. In a previous publication, we took a closer look at how gravitational and Coriolis forces affect dynamical diffraction in crystal interferometry. This paper uses the formalism developed, which allows for extended capabilities in studying the interferometer operation, to investigate numerically the contributions to the neutron phase of geometrical aberrations and dynamical diffraction. In addition, this work explores an alternative geometry, with the interferometer operated vertically, to determine the gravitationally induced quantum-mechanical phase independently of the dynamical diffraction and self-weight bending of the interferometer.

I. INTRODUCTION

Crystal interferometers were developed for x-rays by Bonse and Hart [1,2] and adapted to thermal neutrons by Rauch and coworkers [3]. In these interferometers, a monochromatic x-ray or neutron beam is split by Laue diffraction, recombined by two mirrorlike crystals, and mixed coherently by the last crystal (analyzer). They were used to measure the quantum-mechanical phase resulting from the neutron's interaction with Earth's gravitational field.

In these experiments, known as COW, after Colella, Overhauser, and Werner [4–7], the interference fringes are scanned by tilting the interferometer (while maintaining the Bragg condition) around the incident beam, which remains horizontal. When the interferometer is progressively set up vertically, for instance, with the diffracting planes of the analyzer at a higher gravitational potential than the splitter ones, the momentum of the neutron on the higher arm is lower than that on the lower arm. This results in a difference in the quantum-mechanical phases accumulated by the split wave packets, which is proportional to the area of the interferometer loop.

The bending of the interferometer during the tilting, caused by its weight, poses a challenge. To address it, x-rays were utilized to determine the amount of bending [5,6]. Alternatively, in a related study [7], harmonic pairs of neutron wavelengths were used to measure and correct for it.

It is possible to scan the interference fringes by varying either the crystals' separation [8] or alignment [9,10] of a vertically operating split-crystal interferometer. These scans help to tackle the problems of geometrical aberrations and bending. The metrology and technologies required to detect and control the crystals' displacement and attitude have been developed to measure the lattice parameter of silicon by a split-crystal interferometer, although an order-of-magnitude improvement is necessary [11,12].

Our study focuses on analyzing numerically the quantum interference of neutrons in a geometrically aberrated interferometer for vertical use with split crystals. We did not consider intrinsic mismatching of the diffracting planes and assumed a perfect crystal interferometer. A detailed investigation of the effect of crystallographic imperfections is given in [13].

Our motivation stemmed from the discovery that neutron interference using split-crystal interferometers is feasible [14] and from the observation that the measurements of the gravity-induced phase deviate from the theoretical prediction by approximately 1%, as noted by Littrell and colleagues [7].

The measured value of the interference-fringe phase in Earth's rotating frame is affected by the Sagnac effect and dynamic diffraction in the interferometer crystals. Extensive calculations were performed to apply the necessary corrections [6,13,15–18].

We built upon the previous findings by incorporating the Sagnac effect from first principles, using the transfer-matrix formalism to describe how neutrons propagate between and inside the interferometer crystals while affected by gravitational and Coriolis forces, studying aberrated interferometers, and recalculating how the Coriolis force and dynamic diffraction contribute to the phase difference of the interfering waves.

This paper is organized as follows. Section II summarizes the results of our previous study [8] and provides the basic equations describing the interferometer operation. The formalism, conventional choices, symbols, and notations adopted here are strictly adhered to [8]. To ascertain the visibility and

---

*Contact author: e.massa@inrim.it

†Contact author: g.mana@inrim.it; http://www.fisicamagistrale.unito.it/persone/giovanni.mana

‡Contact author: c.sasso@inrim.it

phase of the tipping and separation interferograms, numerical calculations were performed. The outcomes can be found in Secs. III and IV. Special attention was paid to precisely extracting the gravitational quantum phase from the measured one while accounting for any uncertainty due to geometrical aberrations and dynamical diffraction.

We tested our mathematical formalism and numerical code by replicating the literature values of the phase of the dynamical diffractions [6,7]. The results are given in Sec. III B. Section IV B explores the phase modulation of the neutron interference by varying the split crystals' separation and alignment of the Bragg angle. It shows that separation and angular interferograms are indistinguishable and that dynamical diffraction can be made harmless by rematching in real time the mutual Bragg angle of the split crystals, which, otherwise, the neutrons perceive as mismatched.

All symbolic and numerical calculations were done using *Mathematica* [19]. The relevant notebooks are available in the Supplemental Material [20]. To view and interact with them, WOLFRAM PLAYER can be downloaded [21].

II. NEUTRON INTERFEROMETRY

A. Interferometer model

As illustrated in Fig. 1, the first interferometer crystal splits a neutron beam in two. These separate beams are brought back together in the last crystal, which acts as an analyzer, with the help of two mirrorlike crystals. To vary the phase of the interference fringes, the optical length difference of the interferometer arms must be changed, for example, by rotating an aluminum slab (which acts as a phase modulator) inside the interferometer, tipping the interferometer about the incoming beam, or varying the Bragg angle alignment or separation (in this case, provided the interferometer is set up vertically) of the split crystals. A detailed description of the interferometer operation can be found in our previous paper [8]. Below is a summary of the equations required to compute the visibility and phase of the interference fringes.

The integrated intensity of the $n = o, h$ beam forward transmitted or reflected by the interferometer is

$$I_n = J_n[1 + \Gamma_n \cos(\Phi_n)], \tag{1}$$

where J_n, Γ_n, and Φ_n are the mean count rate, fringe visibility, and phase, respectively. Since it yields the same integrated intensity as a Gaussian Schell model of a partially coherent beam [8,22], we limit ourselves to a coherent Gaussian source $\psi_{\text{in}}(x, y)$ having a radius equal to the coherence length [22,23]. The propagation axis of the incoming beam is assumed to be parallel to the $\mathbf{K}_o$ wave vector satisfying the Bragg condition. We do not model the monochromator used to select the neutron wavelength.

Since the neutron propagation (in both free space and perfect crystals) is separable, if $\psi_{\text{in}}(x, y)$ also is, the integrations over q_y (the momentum conjugate to the y coordinate) needed to calculate I_n can be carried out analytically. The result proves that q_y does not contribute, up to the first order, to the fringe phase. For more information, see Eqs. (26) and (28) in [8]. Therefore, we limit ourselves to two dimensions, x and z, and from now on, we indicate the momentum conjugate to the x coordinate by q.
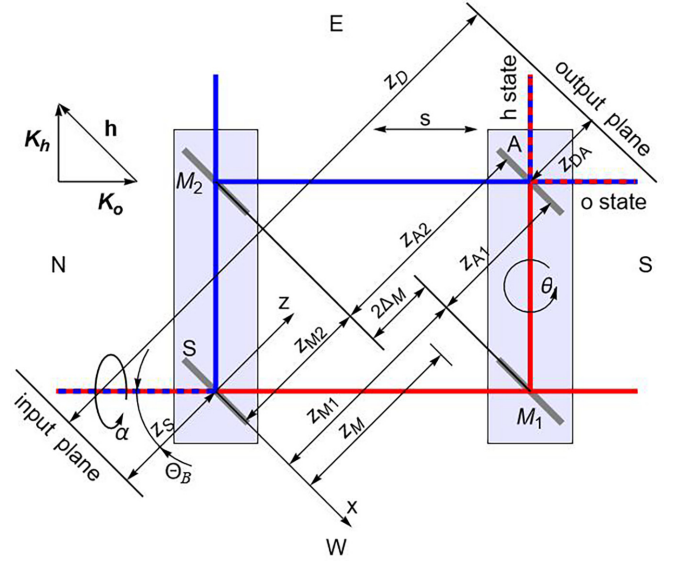

FIG. 1. Crystal interferometer (crystal top view). Abbreviations are as follows: S, splitter; M_1 and M_2, mirrors; A, analyzer. The crystals are plane parallel and symmetrically cut. Red and blue rays indicate the first and second interferometer arms, respectively. The horizontal x axis is orthogonal to the diffracting planes, the crystal vertical y heads inside the drawing, and the optical axis z is normal to the crystals' surfaces. The diffraction geometry is coplanar, with the optical axis lying in the reflection plane. z_S and z_{DA} are the source and detector distances from the splitter and analyzer, respectively. The skewness $2\Delta_M = z_{M2} - z_{M1}$ is the mirrors' gap; z_M is the mirrors' mean distance from the splitter. Θ_B is the Bragg angle; θ is the rotation angle about the crystal vertical. The effective area of the interferometer loop is varied either by tipping the interferometer by the angle α about the incoming beam or by changing the skewness from $2\Delta_M$ to $2\Delta_M + s\cos(\Theta_B)$. The crystal thicknesses are t_S (splitter), t_{M1} and t_{M2} (mirrors), and t_A (analyzer). $\mathbf{h} = -h\hat{\mathbf{x}}$ is the reciprocal vector; the $\mathbf{K}_{o,h}$ wave vectors of the neutron o and h states satisfy the Bragg condition. In the absence of geometrical aberrations (ideal geometry) $t_S = t_A$, $t_{M1} = t_{M2}$, $z_{M1} = z_{A2}$, and $z_{M2} = z_{A1}$.

The mean count rate, visibility, and phase of the integrated interferograms are given by (see [8])

$$J_n \propto \sum_{i=1,2} \int_{-\infty}^{+\infty} |X_{in}(q)\widetilde{\psi}_{in}(q - q_0)|^2 \, dq, \tag{2a}$$

$$\Xi_n \propto \exp[i(f_x \mathcal{A}_0 + f_x \mathcal{A}_1 + h\Delta u + 2f_z \Delta_M \Delta z)]$$
$$\times \int_{-\infty}^{+\infty} e^{iq\Delta x} X_{1n}^*(q) X_{2n}(q) |\widetilde{\psi}_{\text{in}}(q - q_0)|^2 \, dq, \tag{2b}$$

$$\Gamma_n = 2|\Xi_n|/J_n, \tag{2c}$$

$$\Phi_n = \arg(\Xi_n), \tag{2d}$$

where the tilde indicates the Fourier transform, $n = o, h$ is the quantum state of the neutron leaving the interferometer and $i = 1, 2$ is the interferometer arm.

The elements of the transfer matrices propagating the neutrons along the arms of the interferometer are

$$X_{1o}(q) = R(q - q_A; t_A)R(q - q_1; t_{M1})T(q - q_S; t_S), \tag{3a}$$

$$X_{2o}(q) = T(q - q_A; t_A)R(q - q_2; t_{M2})R(q - q_S; t_S), \tag{3b}$$

$$X_{1h}(q) = T(-q + q_A; t_A)R(q - q_1; t_{M1})T(q - q_S; t_S), \quad (3c)$$

$$X_{2h}(q) = R(q - q_A; t_A)R(q - q_2; t_{M2})R(q - q_S; t_S). \quad (3d)$$

The reflection and transmission coefficients, $R(q; t)$ and $T(q; t)$, where t is the crystal thickness, are given in [8].

In (2b), Δz and $2\Delta_M$ are the interferometer defocus (a z translation of the analyzer away from the point where the interferometer arms are recombined) and skewness (the mirrors' gap), respectively, Δx is the x shear of the interfering beams. For a list of the symbols used, refer to Fig. 1 and Appendix F of [8].

Furthermore,

$$\mathcal{A}_0 = 2(t_M z_M + z_{M1} z_{M2} - \Delta_{21}\Delta_M)\tan(\Theta_B) \quad (3e)$$

is the area enclosed by the unperturbed interferometer loop from the splitter to the focus and back,

$$\mathcal{A}_1 = -2(t_A + z_{DA})\Delta z \tan(\Theta_B) \quad (3f)$$

is the area enclosed by the interfering beams from the focus to the detector and back, and

$$\Delta u = -\frac{f_x(t_S^2 + t_A^2 - t_{M1}^2 - t_{M2}^2)\tan(\Theta_B)}{2h} \quad (3g)$$

is the difference between the (splitter, mirrors, and analyzer) diffracting-plane displacements perceived by the free-falling neutron. The $\mathcal{A}_1$ sign opposes the $\mathcal{A}_0$ one because, with a positive defocus, the loop from the focus to the detector is opposite that from the splitter to the focus.

In (3a)–(3d), with a slight abuse of language,

$$\begin{aligned} q_0 &= f_x z_D, \\ q_S &= q_0 - f_x(z_S + t_S/2), \\ q_i &= q_S - f_x(t_S/2 + z_{Mi} + t_{Mi}/2), \\ q_A &= q_i - f_x(t_{Mi}/2 + z_{Ai} + t_A/2) \end{aligned} \quad (4)$$

are the momenta transferred by the gravitational and Coriolis forces acting on the $n = o, h$ states. Note that q_A is independent of the arm along which it is calculated. Here, $\mathbf{f}_n = (f_x, f_{ny}, f_{nz})$ is the pooling of the gravitational and Coriolis forces acting on the $n = o, h$ neutron state, and $\mathbf{f} = (\mathbf{f}_o + \mathbf{f}_h)/2$ and $2\Delta\mathbf{f} = \mathbf{f}_h - \mathbf{f}_o$ are their mean and difference, respectively (see [8]).

To achieve full visibility of interference fringes, the splitter and analyzer must have the same thickness, and so should the two mirrors, i.e., $t_S = t_A$ and $t_{M1} = t_{M2}$. There are two possibilities that are worth considering: $t_S = t_A = t_{M1} = t_{M2}$ and $2t_S = 2t_A = t_{M1} = t_{M2}$. Additionally, a null defocus is necessary. This means that $z_{A1} = z_{M2}$ and $z_{A2} = z_{M1}$. In the $2t_S = 2t_A = t_{M1} = t_{M2}$ case, the interferometer focuses the interfering beams on the exit surface of the analyzer, allowing for good visibility even with a relatively large misalignment of the split crystals.

B. Pooled forces

The pooling of the gravitational and Coriolis forces is given in Appendix B of [8]. Here, we specify the expressions of Earth's gravitational acceleration and angular velocity referring to [5–7].

If the interferometer is rotated counterclockwise about $\mathbf{K}_o = K[\sin(\Theta_B)\hat{\mathbf{x}} + \cos(\Theta_B)\hat{\mathbf{z}}]$ (which is assumed to be horizontal) by the angle α, the acceleration due to Earth's gravity in the interferometer reference frame is

$$\mathbf{g}(\alpha) = \begin{bmatrix} \cos(\Theta_B)\sin(\alpha) \\ \cos(\alpha) \\ -\sin(\Theta_B)\sin(\alpha) \end{bmatrix} g,$$

where $g \approx 9.79978$ m/s^2 at Columbia, Missouri [24]. Note that, when $\alpha = 0$, the crystal vertical points down. We do not discuss a misalignment between the rotation axis and $\mathbf{K}_o$. If misaligned, the $g_x(\alpha)$ acceleration component—the only effective component in our problem—is reduced proportionally to the inclination of the rotation axis relative to the reflection plane [25].

In [5–7], $\mathbf{K}_o$ is oriented from north to south along the local meridian. Therefore, Earth's angular velocity in the interferometer reference frame is

$$\omega = \begin{bmatrix} -\cos(\Theta_B)\cos(\vartheta_L)\sin(\alpha) - \sin(\Theta_B)\sin(\vartheta_L) \\ -\cos(\vartheta_L)\cos(\alpha) \\ \sin(\Theta_B)\cos(\vartheta_L)\sin(\alpha) - \cos(\Theta_B)\sin(\vartheta_L) \end{bmatrix} \omega,$$

where the colatitude angle is $\vartheta_L = 51.37°$ and $\omega \approx 72.7$ µrad/s (counterclockwise about the south to north axis).

III. TIPPING INTERFEROGRAM

To assess the accuracy of the mathematical model in [8] and its numerical implementation, we used Eqs. (2) to quantify the dynamical-diffraction contribution to the fringe phase in the interferometers used by Werner and coworkers [6] and Littrell and coworkers [7]. We focused more on [6] because the data therein are more easily analyzed from the information given.

Our analysis differs from the previous ones [6,15–18] in that we took into account geometrical aberrations and the Coriolis force from first principles. The *Mathematica* code implementing numerically the governing equations is available in the Supplemental Material, part b [20].

A. Measurement equations

When the interferometer is rotated about the incident beam, the measured quantity is the

$$\Phi(\alpha) = f_x \mathcal{A}_0 + f_x \mathcal{A}_1 + h\Delta u + \Phi_D + \Phi_b \quad (5)$$

fringe phase vs the sine function of the tipping angle α. We omitted the subscript indicating the o or h state leaving the interferometer because, due to the absence of absorption, the dynamical phase Φ_D exhibits a difference equal to π independently of α.

The measurement goal is to extract the gravitationally induced phase

$$\Phi_g(\alpha) = \frac{m^2 \mathcal{A}_0 \cos(\Theta_B)\sin(\alpha)g}{\hbar^2 K_z} = \frac{m^2 \mathcal{A}_0 \sin(\alpha)g}{\hbar^2 K}, \quad (6)$$

which is the first term contributing to $f_x \mathcal{A}_0$. Assuming a difference in the mirror thickness $2\Delta_{21}$ of the order of 2 µm

[6], the contribution of $\Delta_{21}\Delta_M$ to the $\mathcal{A}_0$ area [see (3e)] can be neglected.

To describe the propagation of a plane wave, different sign conventions are possible for the phase term, the choice of which has implications for the interpretation of the phase delays. With our convention (see [8]), forward propagation implies that the phase increases with time and decreases with space. Therefore, a positive sign of Φ_g encodes a neutron momentum in the second arm that is lower than the one in the first, as expected.

The second term contributing to $f_x\mathcal{A}_0$,

$$\Phi_S(\alpha) = \frac{2m\mathcal{A}_0\cos(\vartheta_L)\cos(\alpha)\omega}{\hbar}, \tag{7}$$

which is analogous to the Sagnac phase in optics, and the remaining terms of (5) must be quantified and subtracted from $\Phi(\alpha)$.

The Φ_b contribution is due to the self-weight bending of the interferometer: The diffracting planes of the splitter, mirrors, and analyzer mismatch as they are rotated about the incident beam. The discussion of the gravitationally induced strains is outside the scope of the present work. Information is available in [6,7,26].

The Δz defocus shears the interfering beams and changes the area of the interferometer loop from $\mathcal{A}_0$ to $\mathcal{A}_0 + \mathcal{A}_1$. Although the interferometer should have a null defocus, the surface damage removal after cutting causes geometrical imperfections [12]. As per our experience, each crystal deviation from the average thickness is up to at least ± 1 μm, and the defocus is up to at least ± 3 μm. For instance, [6] reported that the tolerance of the blades' thicknesses and their separations is 2 μm. Hence, the propagated defocus tolerance is 6 μm. Figure 2 (top) provides an example of the contribution of the defocus $f_x(\alpha)\mathcal{A}_1$ to the fringe phase.

Owing to the neutron parabolic motion, dynamical diffraction takes the same form as in the case of the propagation in a deformed crystal. The perceived shear strain q_X/K, where $X = S, 1, 2, A$ indicate the splitter, mirrors, and analyzer, is opposite to the angle at which the misset neutron hits the crystals [8] [see (4)]. It makes the phases of the reflection and transmission coefficients dependent on the tipping angle. The implications of this dependence on the dynamical phase Φ_D are discussed in the next section.

In the crystal reference frame, the perceived displacement of the diffracting planes is opposite to half the neutron fall while traversing the crystal [8]. Jointly with nonequal thicknesses of the interferometer crystals, it originates the $h\Delta u(\alpha)$ phase difference between the interfering wave packets given in (3g). As shown in Fig. 2 (bottom), if the same thickness is targeted for all crystals, the ± 2 μm deviations from the average specified in [6] do not cause significant phase excess (defect). Note that this is not true if the design specification of the mirrors' thickness differs from that of the splitter-analyzer pair.

B. Dynamical diffraction

Unwanted phase shifts occur due to the dynamical diffraction in the interferometer crystals, as evidenced by the complex nature of the transmission and reflection coefficients.
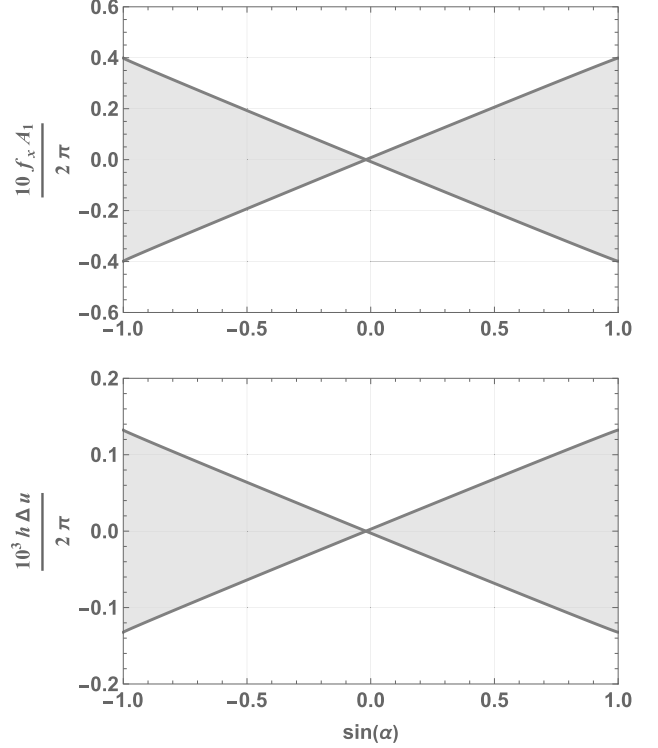

FIG. 2. Distribution (gray area) of the $\mathcal{A}_1 f_x$ (top) and $h\Delta u$ (bottom) phase excesses (defects). They form a bundle of nearly straight lines. The interferometer parameters and 2-μm geometry tolerances are from [6] (see Table I). The detector distance from the interferometer is 0.5 m. The defocus is uniformly distributed in the $[-6, +6]$ μm interval.

The total contribution to the fringe phase,

$$\Phi_D(\alpha) = \arg\left[\int_{-\infty}^{+\infty} e^{iq\Delta x} X_{1n}^*(q)X_{2n}(q)|\widetilde{\psi}_{\text{in}}(q-q_0)|^2 \, dq\right], \tag{8}$$

must be evaluated numerically. Table I gives the physical and geometrical parameters used in the computations.

The Δx shear of the interfering beams arises from both defocusing and skewness. Both contributions are very small, and therefore, the $\exp(iq\Delta x)$ factor will be omitted. See Eq. (23d) in [8] for more information.

The Coriolis forces acting on the h and o states differ in their z components, resulting in different axial momenta transferred to the neutron. This difference originates the $\Delta f_z t^2/2$ offset of the arguments of the crystals' transmission and reflection coefficients (see Eqs. (13a) and (13b) in [8]) and makes the effective crystal thickness different from the geometrical one. For typical interferometers, the thickness excess or defect (see Eq. (9b) in [8]),

$$\Delta t = \frac{\Delta f_z t^2}{2K_z},$$

is a negligibly small fraction of the Pendellösung length. Therefore, we omitted the $\Delta f_z t^2/2$ offset in the numerical computations. With this approximation, the Coriolis force affects the dynamical diffraction only through the x component of the pooled forces.

TABLE I. Parameters used in the numerical computations. The diffracting planes are Si {220}. The 10-nm coherence length is associated with the 0.4° divergence of the incident beam in [6]. The source and detector distances from the interferometer are $z_S = 1.5$ and $z_{DA} = 0.5$ m, respectively. The digits in parentheses are the uncertainties from [6]. To keep the dynamical-theory formalism, we used the dimensionless coefficients $\chi_{0,h}$ of the Fourier expansion of the Fermi pseudopotential; see [8] for more information.

	Shared by all cases	
$\chi_0 = \chi_h = -2.382 \times 10^{-6}$	$n_0 = 1 - 1.191 \times 10^{-6}$	$\mu = 0$
$\ell_0 = 10$ nm	$d = 0.192015$ nm	$h = 32.72$ rad/nm
	Case 1, symmetric geometry [6]	
$t_{M1} = t_{M2} = t_S = t_A = 2.464(2)$ mm	$z_{M1} = z_{M2} = z_{A1} = z_{A2} = 34.518(2)$ mm	$\lambda = 0.1417$ nm
$K = 44.3$ rad/nm	$\Lambda_e = 99.40$ μm	$\Theta_B = 21.65°$
	Case 2, symmetric geometry [7]	
$t_{M1} = t_{M2} = t_S = t_A = 3.077$ mm	$z_{M1} = z_{M2} = z_{A1} = z_{A2} = 50.404$ mm	$\lambda = 0.18796$ nm
$K = 33.4$ rad/nm	$\Lambda_e = 70.31$ μm	$\Theta_B = 29.30°$
	Case 3, skew-symmetric geometry [7]	
$t_{M1} = t_{M2} = t_S = t_A = 2.621$ mm	$z_{M1} = z_{A2} = 49.449$ mm	$z_{M2} = z_{A1} = 16.172$ mm
$\lambda = 0.21440$ nm	$\Lambda_e = 58.64$ μm	$\Theta_B = 33.94°$
	Case 4, split crystal	
$\lambda = 0.27160$ nm	$\Lambda_e = 39.46$ μm	$\Theta_B = 45.00°$
Figure 5		
$t_S = t_A = 2.000$ mm	$t_{M1} = t_{M2} = 2.000$ mm	$z_{M2} = z_{A1} = 10.000$ mm
Figure 6		
$t_S = t_A = 1.000$ mm	$t_{M1} = t_{M2} = 1.000$ mm	$z_{M1} = z_{A2} = 10.000$ mm
Figure 7		
$t_S = t_A = 2.000$ mm	$t_{M1} = t_{M2} = 4.000$ mm	$z_{M1} = z_{A2} = 10.000$ mm

When the tipping angle α was small, we approximated the dynamical phase $\Phi_D(\alpha)$ by assuming ideal geometry (hence, $\Delta x = 0$) and constant $\tilde{\psi}_{in}(q - q_0)$ (i.e., we assumed the spherical wave approximation). Next, we expanded the integrand of (8) around $\alpha = 0$ to first order and averaged the oscillating terms. The symbolic computations can be found in the Supplemental Material, part a [20]. The result,

$$\Phi_D(\alpha) = \frac{16t(t + z_M)}{25(tz_M + z_{M1}z_{M2})} f_x(\alpha)\mathcal{A}_0 + O[\sin^2(\alpha)], \quad (9)$$

where t is the crystals' thickness, is an extension of Eq. (61) in [6] (which applies to the symmetric geometry and gravity alone) to the skew-symmetric geometry and Coriolis force cases.

To reduce the computational load, we assumed the integrands in (2a) and (8) were band limited, sampled the transmission and reflection coefficients in Δq steps according to the Nyquist-Shannon theorem, and used Riemann sums to approximate the integrals. We also approximated the source by a spherical wave; i.e., we assumed $\tilde{\psi}_{in}(q; z = 0) \approx$ const and changed the integration variable from q to $q' = q - q_S$. We evaluated the integrands as products of the samples of the reflection and transmission coefficients shifted to the right or left by the $\lfloor q_X/\Delta q \rceil$ positions, where $X = 1, 2, A$ and the first and last $\lfloor q_A/\Delta q \rceil$ samples are dropped. See the Supplemental Material, part b [20], for more information.

We calculated the contribution $\Phi_D(\alpha)$ of dynamical diffraction to the fringe phase for Werner *et al.*'s and Littrell *et al.*'s interferometers described in [6,7]. Table II compares the experimental and numerical $\Phi_D(\alpha)$ values given in [6,7] with our analytical and numerical results.

Figure 3 (bottom) shows our predictions of the interferograms observed when tilting the symmetric interferometer in [6] (see Table I) by the angle α. The highest visibility,

occurring when the tilt is null, deviates from the expected unity value of 0.3%, which gives a rough idea of the numerical accuracy.

The visibility loss observed away from the zero angle, which corresponds to the horizontal reflection plane, is due to the Bragg misalignments of the diffracting planes perceived by the neutron because of their parabolic motion. These misalignments are encoded in the $q_A - q_S$ and $q_i - q_S$ offsets of the arguments of the reflection and transmission coefficients of the analyzer and mirrors (see (3) and [8,22]).

TABLE II. Comparison of the experimental and numerical values of the fringe phase given in [6,7] with our analytical and numerical results. All values are expressed in radians. The experimental value of the fringe phase Φ (stripped of the phase shift due to the self-weight bending) is obtained from Figs. 5 and 7 of [6].

| Source	Value
	Case 1, symmetric geometry
[6]	analytical $\Phi_D \approx 2.69 \sin(\alpha)$
This paper	analytical $\Phi_D \approx 0.07 + 2.58 \sin(\alpha)$
This paper	numerical $\Phi_D \approx 0.07 + 2.76 \sin(\alpha)$
[6]	experimental $\Phi = 1.48 + 58.69 \sin(\alpha)$
This paper	analytical $\Phi = 1.52 + 59.21 \sin(\alpha)$
	Case 2, symmetric geometry
[7]	numerical $\Phi_D \approx 9.08 \sin(\alpha)$
This paper	analytical $\Phi_D \approx 0.17 + 8.74 \sin(\alpha)$
This paper	numerical $\Phi_D \approx 0.16 + 8.81 \sin(\alpha)$
	Case 3, skew-symmetric geometry
[7]	numerical $\Phi_D \approx 7.03 \sin(\alpha)$
This paper	analytical $\Phi_D \approx 0.12 + 6.75 \sin(\alpha)$
This paper	numerical $\Phi_D \approx 0.10 + 6.75 \sin(\alpha)$
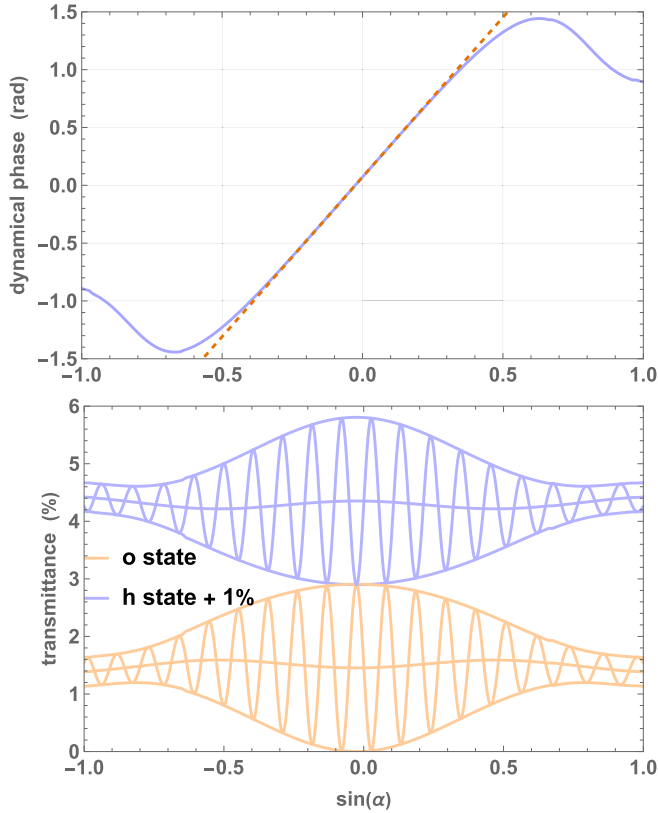
FIG. 3. Top: dynamical diffraction phase Φ_D; the orange line is the best linear fit in the $[-0.025, +0.025]$ interval of $\sin(\alpha)$. Bottom: tipping interferograms. The parameters used are for the symmetric interferometer in [6] (see Table I).

Our approach to the dynamical diffraction differs from those of Bonse and Wroblewski [16] and Horne [17]. A comparison between Fig. 3 (bottom) and Werner *et al.*'s Fig. 11 in [6] reveals that the predictions are essentially the same. However, contrary to Bonse and Wroblewski's and Horne's dynamical calculations, our model includes the Coriolis force, which results in a phase shift of approximately 1.5 rad.

In Fig. 3 (top), we display our forecasted value of the dynamical phase Φ_D for the same interferometer. This phase is similar to that observed by rocking the analyzer of a split-crystal interferometer used to measure the lattice parameter of silicon, as reported in [27] and explained theoretically in [28,29].

We compared Fig. 3 (top) with Werner *et al.*'s Fig. 12 [6] and Heacock *et al.*'s Fig. 8 (top) [13] (see also Table II). The agreement is good; the opposite sign is due to the opposite tipping directions. Our Φ_D linearization at $\alpha = 0$ [see (9)] is $0.07 + 2.58 \sin(\alpha)$ rad. The more accurate numerical one is $0.07 + 2.84 \sin(\alpha)$ rad. Werner *et al.*'s linearization is $2.70 \sin(\alpha)$ rad (see Table II and Eq. (61) in [6]). In contrast to us, they found $\Phi_D(\alpha = 0) = 0$. These differences are due to our inclusion of the Coriolis force in the interferometer model and, consequently, to the different crystal misalignments perceived by the neutron.

We obtained Werner *et al.*'s experimental value of the fringe phase from Fig. 5 in [6]. After removing the phase shift due to the self-weight bending reported in Fig. 7 of
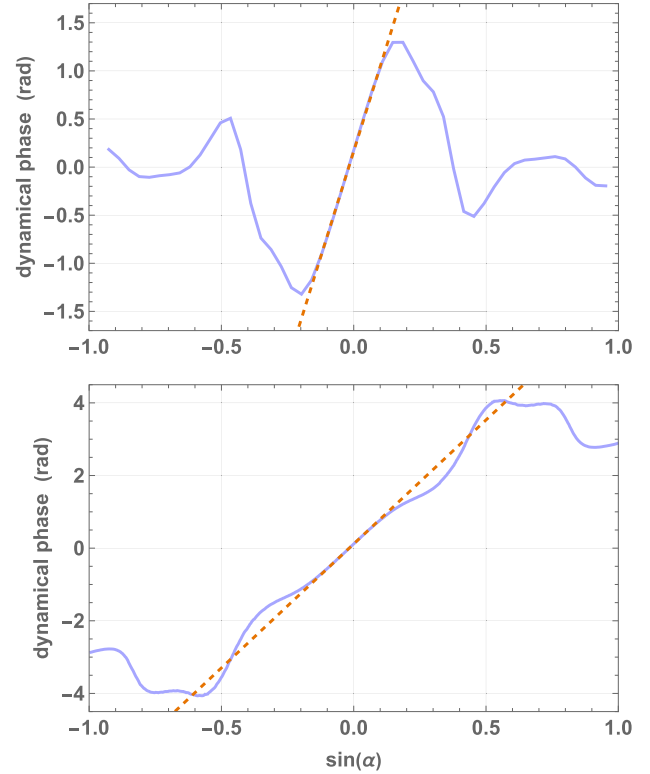

FIG. 4. Dynamical diffraction phase Φ_D. Littrell's symmetric (top) and skew-symmetric (bottom) interferometers (see [7] and Table I). The orange line is the best linear fit in the $[-0.025, +0.025]$ interval of $\sin(\alpha)$.

[6], $\Phi_b(\alpha) = 1.41 \sin(\alpha)$ rad, we obtained $\Phi(\alpha) = [1.48 + 58.69^{+0.25}_{-0.25} \sin(\alpha)]$ rad. The uncertainty margins are the upper and lower limits of $f_x \mathcal{A}_1$'s, which are shown in Fig. 2. Our simulated value of the fringe phase is $\Phi(\alpha) = [1.52 + 59.21 \sin(\alpha)]$ rad.

Figure 4 displays our $\Phi_D(\alpha)$ outcomes in the cases of the symmetric and skew-symmetric interferometers described in [7]. Table II compares our Φ_D approximations in the neighborhood of $\alpha = 0$ and those estimated from Fig. 16 of [7], which gives the Φ_D/Φ_g ratios. We used a web-based digitization tool [30] to recover the 4.06% (symmetric geometry) and 6.99% (skew-symmetric geometry) ratio values.

IV. SEPARATION INTERFEROGRAM

This section explores the working of the split interferometer when it is operated vertically. The *Mathematica* code numerically implementing the governing equations is available in the Supplemental Material, part c [20].

A. Measurement equations

As shown in Fig. 1, by using a vertically operating split-crystal interferometer, the interference can be modulated by varying either the skewness from $2\Delta_M$ to $2\Delta_M + \cos(\Theta_B)s$, where s is a displacement parallel to the incident beam, or the crystals' misalignment θ in the reflection plane (the mutual rotation angle about the y axis of the split crystals, as shown in Fig. 1).

Since the crystal separation and rotation do not affect the (perceived) crystal strains and self-weight bending, the $h\Delta u$ and Φ_b terms of the fringe phase (5) can be disregarded. Hence, we rewrite (5)–(7) as

$$\Phi(s) = f_x \mathcal{A}'_0 + f_x \mathcal{A}'_1 + \Phi_D + h u_\theta, \tag{10a}$$

$$\Phi_g(s) = -\frac{m^2 \mathcal{A}'_0(s) \cos(\Theta_B) g}{\hbar^2 K_z}, \tag{10b}$$

and

$$\Phi_S(s) = -\frac{2m \mathcal{A}'_0(s) \cos(\vartheta_L) \omega}{\hbar}. \tag{10c}$$

The areas of the interferometer loops depend on the crystal separation and are now given by

$$\mathcal{A}'_0(s) = \mathcal{A}_0 + (t_M + 2z_{M2}) \sin(\Theta_B) s \tag{10d}$$

and

$$\mathcal{A}'_1(s) = \mathcal{A}_1 + 2\Delta z \sin(\Theta_B) s. \tag{10e}$$

The last term of (10a),

$$h u_\theta = h(z_{A1} + t_{M1}/2)\theta, \tag{10f}$$

was not previously accounted for. The dependence on θ of the interferometer operation is a peculiar characteristic of the skew-symmetric geometry [9,10]. Accordingly, when the Bragg alignment of the split crystals is varied, interference fringes are produced with a periodicity equal to

$$\Lambda_\theta = \frac{d}{z_{A1} + t_{M1}/2}. \tag{}$$

In Eqs. (3), assuming that the incident beam satisfies the Bragg condition on the splitter, the transferred momentum q_S is zero. Mathematically, this corresponds to redefining the q mode as $q = q' + q_S$. Also, the integrals in (2a), (2b), and (8) can be equally solved with respect to either q or $q' + q_S$. Consequently, omitting the prime, we rewrite Eqs. (3) as

$$X_{1o}(q + q_S) = R(q - q_A + q_\theta; t_A) R(q - q_1 + q_\theta; t_{M1})$$
$$\times T(q; t_S), \tag{11a}$$

$$X_{2o}(q + q_S) = T(q - q_A + q_\theta; t_A) R(q - q_2; t_{M2})$$
$$\times R(q; t_S), \tag{11b}$$

$$X_{1h}(q + q_S) = T(-q + q_A - q_\theta; t_A) R(q - q_1 + q_\theta; t_{M1})$$
$$\times T(q; t_S), \tag{11c}$$

$$X_{2h}(q + q_S) = R(q - q_A + q_\theta; t_A) R(q - q_2; t_{M2}) R(q; t_S), \tag{11d}$$

where $q_\theta = \theta K_z$ is the momentum associated with the rotation angle θ of the second crystal relative to the first. Similarly, Eqs. (4) are rewritten as (see [20])

$$q_0 = f_x(z_S + t_S/2),$$
$$q_1(s) = -f_x[t_S/2 + z_{M1} + t_{M1}/2 + s\cos(\Theta_B)],$$
$$q_2(s) = -f_x(t_S/2 + z_{M2} + t_{M2}/2),$$
$$q_A(s) = -f_x[z_T + s\cos(\Theta_B)], \tag{12}$$

where $z_T = t_S/2 + z_{Mi} + t_{Mi} + z_{Ai} + t_A/2$ is the distance (center to center) of the analyzer from the splitter.

By rotating the second crystal about its vertical, we can eliminate, for instance, the deviation from the Bragg condition of mirror 1 or the analyzer. In the second case, in Eqs. (11),

$$q_1(s) + q_\theta = f_x[t_{M1}/2 + z_{A1} + t_A/2 - s\cos(\Theta_B)] + \theta_A K_z$$
$$\stackrel{\text{ideal}}{=} -q_2 - f_x s\cos(\Theta_B) + \theta_A K_z,$$
$$q_A(s) + q_\theta = -f_x s\cos(\Theta_B) + \theta_A K_z, \tag{13}$$

where θ_A is the analyzer rotation angle away from the angle $\theta = f_x z_T / K_z$ compensating for the analyzer misalignment and the overscript on the equal sign indicates the ideal geometry. After we adjust for this compensation, the deviations from the Bragg condition of the interferometer crystals are not affected by the $s = 0$ skewness. It is important to note that the crystals' gap needs to accommodate an optical interferometer to sense their alignment [31,32]. Therefore, the fact that the initial skewness does not impact the interferometer operation is a valuable characteristic.

Once the analyzer misalignment associated with the initial skewness has been compensated, the residual crystals' misalignments depend on only the separation of the interferometer arms. A little separation results in fewer misalignments and higher visibility. However, the sensitivity of the gravitationally induced phase to the displacement s is twice as much proportional to this separation, as seen in (10d). Therefore, larger values are better. Ultimately, there is a need to balance between small and large separations.

The phases induced by the displacement s [see (10d)] and the rotation θ [see (10f)] can be rewritten as

$$f_x(A'_0 - \mathcal{A}_0) = f_x(t_M + 2z_{M2}) \sin(\Theta_B) s$$
$$= K_z(t_M + 2z_{M2}) \sin(\Theta_B)\theta, \tag{14a}$$

where $\theta = f_x s / K_z$ is the propagation-direction change of the neutrons impinging the analyzer, and associated with the displacement s, and

$$h u_\theta = h(z_{A1} + t_{M1}/2)\theta = K_z(t_M + 2z_{M2}) \sin(\Theta_B)\theta, \tag{14b}$$

where we used $2h = K_z \sin(\Theta_B)$ and neglected the geometrical aberrations. Upon comparing (14a) and (14b), it becomes evident that the second crystal displacement and rotation are indistinguishable. Accordingly, the gravitational phase is accounted for equally well by the difference in the neutron momenta in the highest and lowest arms and the neutron perception of the crystals' mismatch due to its fall in the gravitational field.

Assuming ideal geometry, if the displacement-induced phase is compensated online by that due to the rotation angle

$$\theta(s) = \frac{f_x s}{K_z} = \frac{f_x \sin(\Theta_B) s}{2h}, \tag{15}$$

the fringe phase (10a) does not change. Therefore, the gravitationally induced phase can be determined by measuring the rotation $\theta(s)$ locking the interference phase to a constant value, provided the angle measurement has been calibrated. It is worth noting that this measurement procedure allows the gravitationally induced phase to be determined independently of dynamical diffraction.
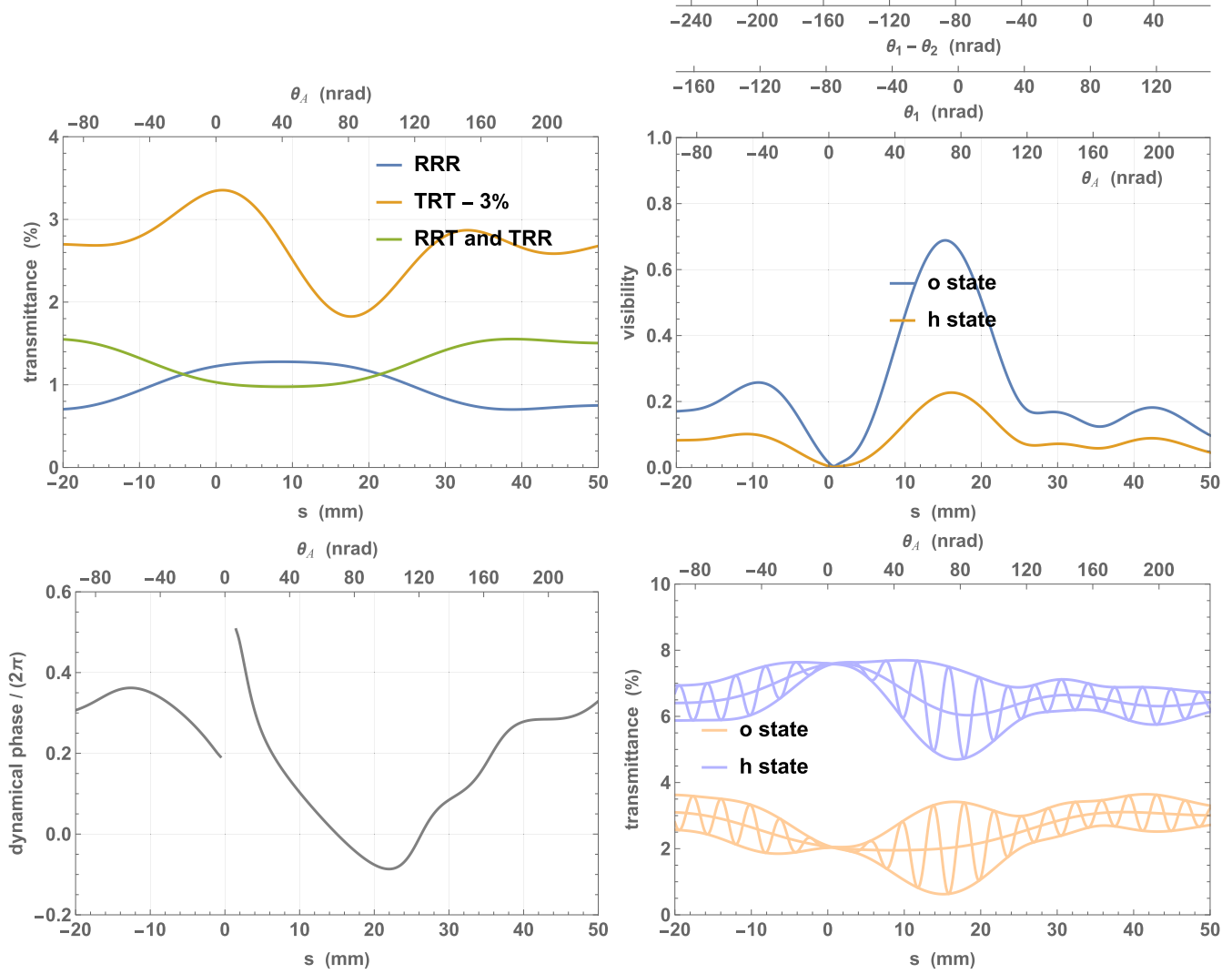
FIG. 5. Rocking curves (top left), visibility (top right), dynamical diffraction phase (bottom left), and interferograms (bottom right) of a split-crystal interferometer set vertically. s and θ_A are the second crystal displacement and rotation angle away from the angle that compensates the $s = 0$ deviation (perceived by the neutron) of the analyzer from the Bragg alignment. θ_1 and θ_2 are the perceived deviations from the Bragg alignment of mirrors 1 and 2. RRR, TRT, RRT, and TRR indicate the sequences of reflections (R) and transmissions (T) by the splitter, mirrors, and analyzer. The crystal thicknesses are $t_S = t_{M1} = t_{M2} = t_A = 2$ mm. The parameters used in the computations are given in Table I.

B. Dynamical diffraction

Figures 5–7 show the predicted operation of split-crystal interferometers set vertically when displacing (bottom axis) or rotating (top axis) the second crystal. Three cases are shown, each with different splitter, mirror, and analyzer thicknesses but identical geometries otherwise. For more details on the parameters used in the computations, refer to Table I.

To minimize the perceived misalignments and maximize the interference visibility, the separation of the interferometer arms was set to 10 mm, i.e., $z_{M2} = z_{A1} = 10$ mm. Furthermore, we assumed that the analyzer misalignment associated with the initial $2\Delta_M(s = 0)$ skewness was compensated. Therefore, in Figs. 5–7, the origins of the s (bottom axis) and θ_A (top axis) scales are the same.

According to (14a) and (14b), the second crystal rotation, $\theta_A = f_x s / K_z$, is equivalent to the displacement $s = K_z \theta_A / f_x$ and vice versa. Here, the word "equivalent" means that both

cause the same Bragg mismatch and induce the same phase shift between the interfering beams. Therefore, in Figs. 5–7, the top axes give the deviations from the exact Bragg alignment of the analyzer and mirror 1 (θ_A and θ_1, respectively) associated with the displacement s shown on the bottom axis. The mismatch between mirrors 1 and 2 is also given.

The initial skewness $2\Delta_M(s = 0)$ is irrelevant. In fact, Eqs. (13) are independent of z_{M1} and z_{A2}. Therefore, the results shown in Figs. 5–7 hold for any $2\Delta_M(s = 0)$ value.

Different sets of crystal thickness were considered: $t_S = t_A = t_{M1} = t_{M2} = 2$ mm (Fig. 5), $t_S = t_A = t_{M1} = t_{M2} = 1$ mm (Fig. 6), and $2t_S = 2t_A = t_{M1} = t_{M2} = 4$ mm (Fig. 7). In the latter case, we expected good visibility over relatively large Bragg misalignments. Figure 6 confirms that, in this case, the interferogram visibility is insensitive to the second crystal separation and misalignment but also that it is small everywhere.
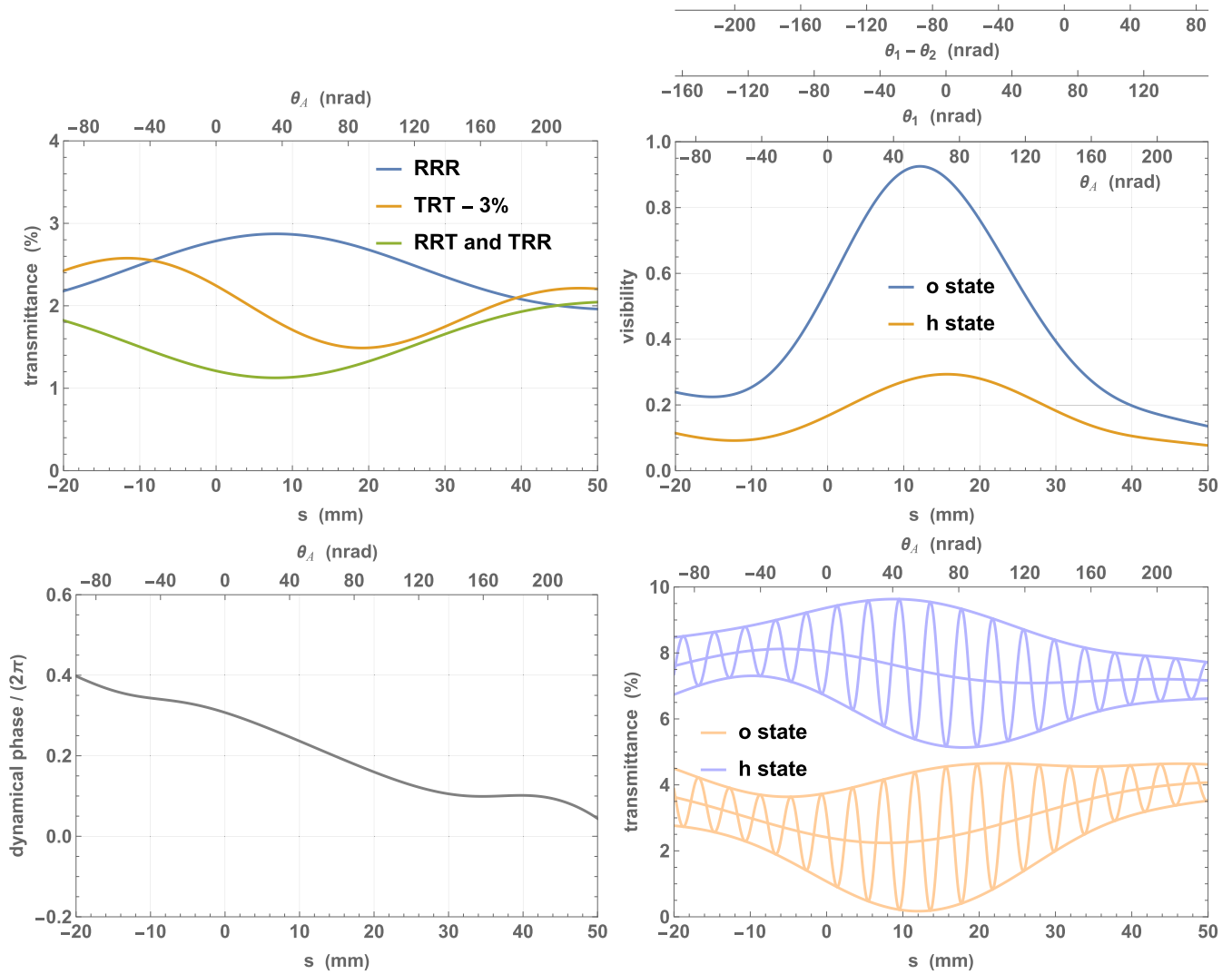
FIG. 6. Rocking curves (top left), visibility (top right), dynamical diffraction phase (bottom left), and interferograms (bottom right) of a split-crystal interferometer set vertically. s and θ_A are the second crystal displacement and rotation angle away from the angle that compensates the $s = 0$ deviation (perceived by the neutron) of the analyzer from the Bragg alignment. θ_1 and θ_2 are the perceived deviations from the Bragg alignment of mirrors 1 and 2. RRR, TRT, RRT, and TRR indicate the sequences of reflections (R) and transmissions (T) by the splitter, mirrors, and analyzer. The crystal thicknesses are $t_S = t_{M1} = t_{M2} = t_A = 1$ mm. The parameters used in the computations are given in Table I.

The rocking curves are given as ratios between the fluxes of the neutrons leaving the interferometer and the flux of the incoming ones. Due to the interferometer's limited angular acceptance, the transmittances depend on the angular width of the initial state. The larger the angular width is, the smaller the transmittances are. The values given in Figs. 5–7 refer to the initial state given in Table I. Since the absorption is null, the RRT and RRR transmittances—this notation indicates the sequences of reflections (R) and transmissions (T) by the splitter, mirrors, and analyzer—total to a constant. Because of the same null absorption the o- and h-state interferograms are in counterphase.

In the absence of geometrical imperfections, the TRR and RRT flux ratios are identical (see Figs. 5–7). This is because of the symmetries of the reflection and transmission coefficients, and, in (11a) and (11b), $q_A(s) - q_1(s) = q_2$. The

symbolic proof can be found in the Supplemental Material, part a [20].

When the visibility is null, the complex amplitude of the interference fringes $\Xi_n(s)$ crosses the zero. The reversing of the $\Xi_n(s)$ sign corresponds to a π discontinuity of the dynamical phase, as shown in Fig. 5. Also, since the o- and h-state interferograms are constrained to be in counterphase, zero visibility always happens simultaneously in the o and h states.

Figures 5 and 6 indicate that visibility is maximum when the displaced mirror is approximately aligned, and thin crystals improve fringe visibility and expand the interferometer's working ranges. Since it is impossible to investigate this clue analytically, we focused on a simulation sequence with increasing thicknesses. The results, shown in Fig. 8, confirm what the clue hinted at. It is worth noting that the man-
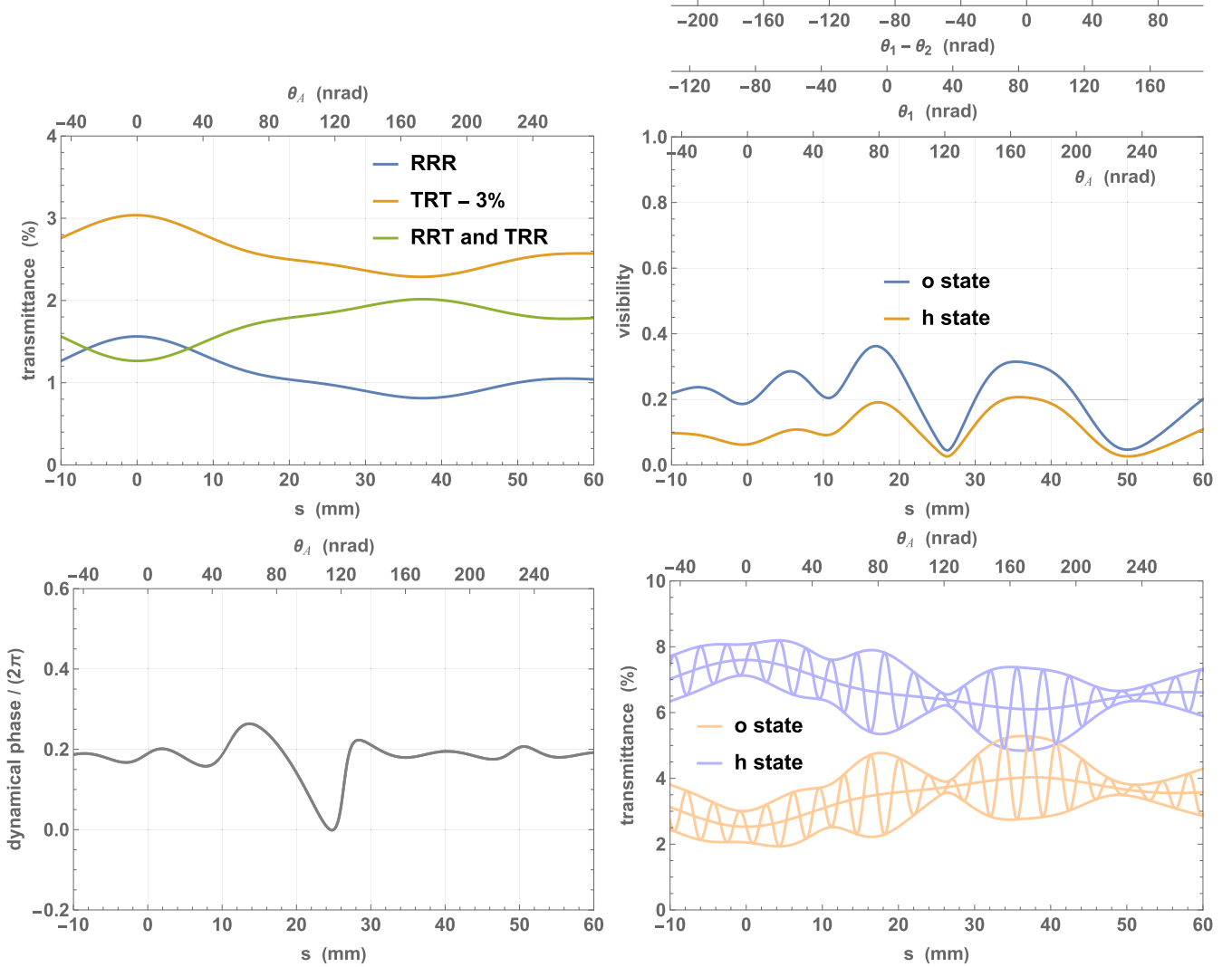
FIG. 7. Rocking curves (top left), visibility (top right), dynamical diffraction phase (bottom left), and interferograms (bottom right) of a split-crystal interferometer set vertically. s and θ_A are the second crystal displacement and rotation angle away from the angle that compensates the $s = 0$ deviation (perceived by the neutron) of the analyzer from the Bragg alignment. θ_1 and θ_2 are the perceived deviations from the Bragg alignment of mirrors 1 and 2. RRR, TRT, RRT, and TRR indicate the sequences of reflections (R) and transmissions (T) by the splitter, mirrors, and analyzer. The crystal thicknesses are $2t_S = t_{M1} = t_{M2} = 2t_A = 4$ mm. The parameters used in the computations are given in Table I.

ufacturing and operation of interferometers with 0.56- and 0.98-mm-thick crystals are reported in [33,34].

V. CONCLUSIONS

To effectively use crystal neutron interferometry in metrology, it is necessary to understand the effects of gravity, Coriolis forces, crystal transmission and reflection, and geometric imperfections on the neutron wave function. We developed a mathematical model based on the transfer-matrix formalism. It integrates geometry aberration, three-dimensional propagation, incoherent sources, gravity, and the Coriolis force from first principles.

To ensure that our model and its numerical implementation are accurate, we replicated the simulations of the COW experiment found in the literature. Additionally, we assessed the uncertainties and systematic errors caused by interferometer

deviations from geometrical perfection. Although an accurate evaluation would require knowledge of the interferometer geometry, we did not find clues that could explain the observed discrepancy in addition to the crystallographic imperfections reported in [13].

The two most significant aberrations are the defocus and nonequal thicknesses of the interferometer crystals. The first alters the effective area of the interferometer loop. It can be made harmless by minimizing the detector distance from the interferometer. The second is relevant only if the mirrors' thickness is designed differently from that of the splitter-analyzer pair. This design causes a difference, which depends on the tipping angle, between the perceived mirrors' strains and those of the splitter and analyzer pair.

We calculated the dynamical contribution to the neutron phase and extended its approximation about a null tipping angle to the skew-symmetric geometry. Our result aligns with
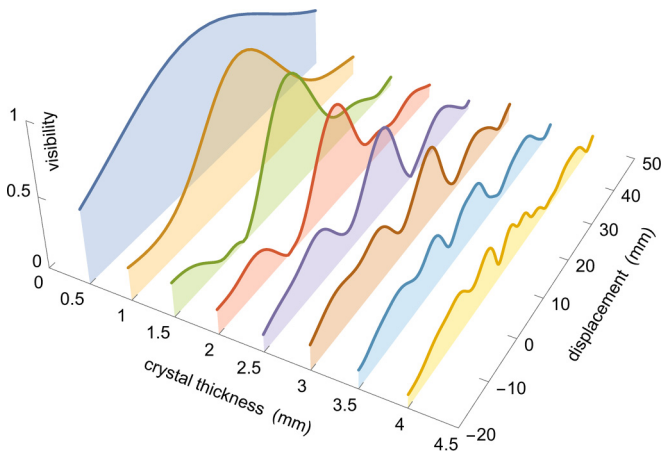
FIG. 8. Ridgeline plot of the visibility of the separation interferogram (*o* state) of a split-crystal interferometer operating vertically vs the crystals' thickness. The perceived $s = 0$ misalignment of the analyzer has been compensated. The parameters used in the calculations are given in Table I.

the existing literature, with a slight difference because we included *ab initio* the Coriolis force in the interferometer model.

We investigated the vertical operation of a split-crystal interferometer. Changing the separation of the crystals to vary the gravity-induced phase difference eliminates uncertainties

and systematic errors caused by geometric imperfections and self-weight strain due to gravity.

The neutrons fall through the free space between the split crystals, causing them to appear misaligned. However, they can be realigned by rotating them around the normal to the reflection plane. This means that the gap between the crystals does not impact the interference visibility, which is determined by only the thickness of the crystals and the separation of the interferometer arms. Thinner crystals result in better visibility.

We proved that varying the crystals' distance is indistinguishable from varying their mutual alignment. Therefore, the gravity-induced phase difference can be compensated and measured using a feedback loop keeping the crystals aligned. It is worth noting that this procedure eliminates any dynamical contribution to the measurement.

[1] U. Bonse and M. Hart, Principles and design of Laue-case x-ray interferometers, Z. Phys. **188**, 154 (1965).

[2] U. Bonse and M. Hart, An x-ray interferometer, Appl. Phys. Lett. **6**, 155 (1965).

[3] H. Rauch, W. Treimer, and U. Bonse, Test of a single crystal neutron interferometer, Phys. Lett. A **47**, 369 (1974).

[4] R. Colella, A. W. Overhauser, and S. A. Werner, Observation of gravitationally induced quantum interference, Phys. Rev. Lett. **34**, 1472 (1975).

[5] J. L. Staudenmann, S. A. Werner, R. Colella, and A. W. Overhauser, Gravity and inertia in quantum mechanics, Phys. Rev. A **21**, 1419 (1980).

[6] S. Werner, H. Kaiser, M. Arif, and R. Clothier, Neutron interference induced by gravity: New results and interpretations, Phys. B+C (Amsterdam) **151**, 22 (1988).

[7] K. C. Littrell, B. E. Allman, and S. A. Werner, Two-wavelength-difference measurement of gravitationally induced quantum interference phases, Phys. Rev. A **56**, 1767 (1997).

[8] C. P. Sasso, G. Mana, and E. Massa, preceding paper, Gravitational and Coriolis forces in crystal neutron interferometry. I. Theory, Phys. Rev. A **110**, 062818 (2024).

[9] D. Windisch and P. Becker, Angular measurements with x-ray interferometry, J. Appl. Crystallogr. **25**, 377 (1992).

[10] U. Kuetgens and P. Becker, X-ray angle interferometry: A practical set-up for calibration in the microrad range with nanorad resolution, Meas. Sci. Technol. **9**, 1072 (1998).

[11] L. Ferroglio, G. Mana, and E. Massa, Si lattice parameter measurement by centimeter x-ray interferometry, Opt. Express **16**, 16877 (2008).

[12] E. Massa, G. Mana, U. Kuetgens, and L. Ferroglio, Measurement of the lattice parameter of a silicon crystal, New J. Phys. **11**, 053013 (2009).

[13] B. Heacock, M. Arif, R. Haun, M. G. Huber, D. A. Pushin, and A. R. Young, Neutron interferometer crystallographic imperfections and gravitationally induced quantum interference measurements, Phys. Rev. A **95**, 013840 (2017).

[14] H. Lemmel, M. Jentschel, H. Abele, F. Lafont, B. Guerard, C. P. Sasso, G. Mana, and E. Massa, Neutron interference from a split-crystal interferometer, J. Appl. Crystallogr. **55**, 870 (2022).

[15] S. A. Werner, Gravitational and magnetic field effects on the dynamical diffraction of neutrons, Phys. Rev. B **21**, 1774 (1980).

[16] U. Bonse and T. Wroblewski, Dynamical diffraction effects in noninertial neutron interferometry, Phys. Rev. D **30**, 1214 (1984).

[17] M. A. Horne, Neutron interferometry in a gravity field, Phys. B+C (Amsterdam) **137**, 260 (1986).

[18] K. C. Littrell, B. E. Allman, O. I. Motrunich, and S. A. Werner, The effects of dynamical diffraction on the measurement of gravitationally induced quantum phase shifts by neutron interferometry, Acta Crystallogr., Sect. A **54**, 563 (1998).

[19] Wolfram Research, Inc., *Mathematica*, version 13.3, Wolfram Research, Champaign, IL, 2023.

[20] See Supplemental Material at http://link.aps.org/supplemental/10.1103/PhysRevA.110.062819 for the symbolic computation (part a), the numerical implementation of section III (part b), and the numerical implementation of section IV (part c).

[21] Wolfram Research, Inc., WOLFRAM PLAYER, version 12.3.1, Wolfram Research, Champaign, IL, 2023.

[22] C. P. Sasso, G. Mana, and E. Massa, Three-dimensional model of a split-crystal x-ray and neutron interferometer, J. Appl. Crystallogr. **55**, 1500 (2022).

[23] C. P. Sasso, G. Mana, and E. Massa, A skew-symmetric split-crystal neutron and x-ray interferometer, J. Appl. Crystallogr. **57**, 44 (2024).

[24] Wolfram Research, Inc., WOLFRAM—ALPHA NOTEBOOK EDITION, version 13.3, Wolfram Research, Champaign, IL, 2023.

[25] H. Lemmel (private communication).

[26] H. P. Layer and G. L. Greene, Elastic deformation of a monolithic perfect crystal interferometer: Implications for gravitational phase shift experiments, Phys. Lett. A **155**, 450 (1991).

[27] G. Basile, A. Bergamin, G. Cavagnero, G. Mana, and G. Zosi, Progress at IMGC in the absolute determination of the silicon d220 lattice spacing, IEEE Trans. Instrum. Meas. **38**, 210 (1989).

[28] G. Mana and E. Vittone, LLL x-ray interferometry. I Theory, Z. Phys. B **102**, 189 (1997).

[29] G. Mana and E. Vittone, LLL x-ray interferometry. II Aberration analysis, Z. Phys. B **102**, 197 (1997).

[30] A. Rohatgi, WEBPLOTDIGITIZER, version 4.6 (2022).

[31] J. Krempel, A new spectrometer to measure the molar Planck constant, Ph.D. thesis, Ludwig-Maximilians Universität München, 2011.

[32] E. Massa, G. Mana, J. Krempel, and M. Jentschel, Polarization delivery in heterodyne interferometry, Opt. Express **21**, 27119 (2013).

[33] P. Becker, U. Bonse, A. Dettmer, F. Dubus, and M. Zawisky, Neutron interferometer with very thin lamellae, Cryst. Res. Technol. **36**, 589 (2001).

[34] E. Massa, G. Mana, U. Kuetgens, and L. Ferroglio, Calibration of a silicon crystal for absolute nuclear spectroscopy, J. Appl. Crystallogr. **43**, 293 (2010).